Fully Coupled Aeroelastic Stability Analysis of Adaptive Shape Memory Alloy Structural Technologies for Airframe Noise Reduction

Michael R. Nucci[1], Eric L. Blades[2], Nicolas D. Reveles[3], and Parthiv N. Shah[4]
ATA Engineering, Inc., San Diego, CA, 92128, USA

Travis L. Turner[5] and David P. Lockard[6]
NASA Langley Research Center, Hampton, VA, 23681, USA

The objective of this work is the development of computational models and analysis of the coupled fluid-structure response of a slat gap filler (SGF) noise treatment applied to the leading-edge slat component of a high-lift system typical of modern transport aircraft. The representative airframe chosen for this work is the NASA-Boeing High-Lift Common Research Model (CRM-HL) in a baseline high-lift configuration. Superelastic shape memory alloys (SMAs) have been identified as enabling materials for these structural treatments. Since the technology elements rely upon having a highly reconfigurable structure, designs must be assessed for static aeroelastic deflection as well as dynamic aeroelastic stability using coupled computational fluid dynamics (CFD) and nonlinear computational structural dynamics (NL-CSD) tools. The technical approach consists of solving for the flow field around the entire vehicle using a global CFD model, followed by extraction of relevant local subdomain data for CFD and NL-CSD cosimulations. The SGF design is assessed using both 2D and 3D co-simulations to predict quasi-static aeroelastic deformations and to assess dynamic aeroelastic stability.

I. Nomenclature

a	=	speed of sound
C	=	stress influence coefficient
CFD	=	computational fluid dynamics
CRM-HL	=	High-Lift Common Research Model
CSD	=	computational structural dynamics
CSE	=	Cosimulation Engine
E	=	Young's modulus
FSI	=	fluid-structure interaction
$\vec{F}_w$	=	force vector
H	=	transformation strain
M	=	Mach number
NiTi	=	nitinol
NL-CSD	=	nonlinear CSD
P	=	pressure
q, Q	=	dynamic pressure
t	=	time
SGF	=	slat gap filler
SMA	=	shape memory alloy

[1] Senior Project Engineer, 13290 Evening Creek Dr S, San Diego, CA 92128
[2] Vice President and Technical Fellow, AIAA Associate Fellow, 1500 Perimeter Pkwy, Ste 285, Huntsville, AL 35806
[3] Senior Project Engineer, AIAA Senior Member, 1500 Perimeter Pkwy, Ste 285, Huntsville, AL 35806
[4] Senior Technical Advisor, AIAA Associate Fellow, 13290 Evening Creek Dr S, San Diego, CA 92128
[5] Aerospace Technologist, AIAA Associate Fellow, 1 Nasa Dr, Hampton, VA 23666
[6] Aerospace Technologist, AIAA Associate Fellow, 1 Nasa Dr, Hampton, VA 23666

T	=	temperature	ζ	=	damping coefficient
$\vec{T}_w$	=	traction vector	ν	=	Poisson's ratio
U_j	=	deformation in the j^{th} axis	σ	=	stress
V	=	velocity	Ω_{base}	=	(constant) natural frequency
$\vec{x}_w$	=	displacement vector	Ω_{vary}	=	frequency sensitivity coefficient
y	=	second-order system response	ω	=	time-dependent frequency
ε	=	strain			

II. Introduction

Aircraft noise reduction is an important goal for the NASA Advanced Air Transport Technology Project. During the approach and landing phases of flight, nonpropulsive (or airframe) noise is a priority because its contribution to overall noise is roughly equal to that of the propulsion system. Airframe noise includes noise from aeroacoustic sources associated with the high-lift system (e.g., the leading-edge slats, trailing-edge flaps, and the aircraft undercarriage). The ranking of airframe noise sources is configuration-dependent, but both model-scale tests [1]–[7] and flyover noise measurements [8] have identified the leading-edge slat as a prominent source of airframe noise during aircraft approach.

The separated, multielement configuration of high-lift systems for typical transport aircraft enables greater lift and lower speeds than single-element systems. However, geometric discontinuities such as gaps, edges, and cavities cause substantial flow unsteadiness and, consequently, aeroacoustic noise. One concept that has been proposed for leading-edge slat noise reduction is a slat gap filler (SGF) [9]. Fig. 1 shows the typical gap throughflow in the slat region of an airfoil and a schematic depiction of an SGF used to mitigate associated aeroacoustic noise. The SGF blocks the gap flow and creates a large recirculation region between the slat and main wing that produces aerodynamics equivalent to the baseline high-lift configuration and aeroacoustics equivalent to drooped-leading-edge (DLE) concepts at angles of attack typical of aircraft operations. In anomalous or emergency conditions, and in contrast to DLE concepts, the SGF represents a small structural modification that can be readily opened to return to the baseline high-lift configuration when needed. Previous work has demonstrated the feasibility of the SGF concept [9] and the noise-reduction potential of the device [10] for a pseudo-2D model (spanwise-uniform section).

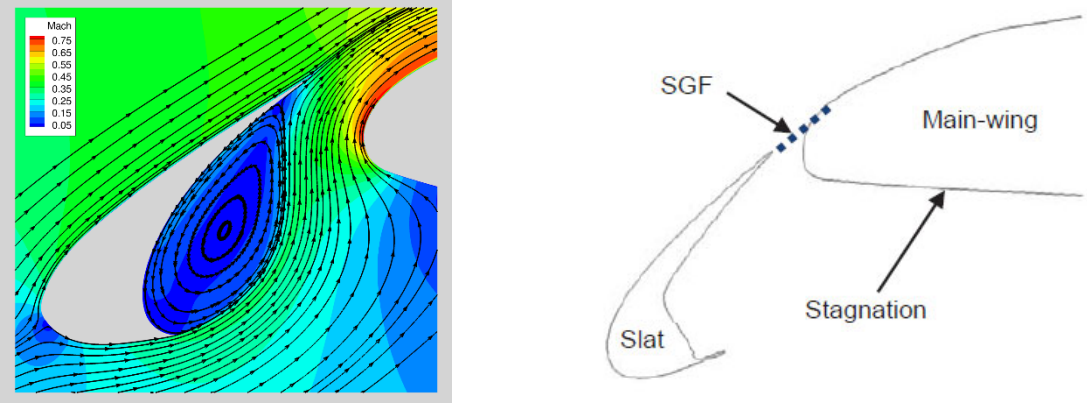

Fig. 1 Gap throughflow seen in streamlines in slat region of a conventional airfoil (left) is an aeroacoustic source that can be mitigated with an SGF (right). Images adapted from reference [9].

Shape memory alloy (SMA) materials have been identified as enabling for this structural treatment approach [9] with practical realization dependent on having a highly reconfigurable structure. Although it has been shown that a conventional material could achieve the requirements of the SGF for a portion of the airframe for a typical transport aircraft, the unique properties of SMA materials are required for much of the airframe due to the large strain requirement. SMAs are advantageous even in regions where conventional materials are relevant due to properties like corrosion resistance, hardness, and (most importantly) tailorability for reduction of articulation forces.

NASA has constructed a 10% scale version of the High-Lift Common Research Model (CRM-HL) developed by Lacy and Sclafani [11] for further development of airframe noise-reduction technologies. The original cruise-configuration NASA CRM is an open geometry that has been widely used in the AIAA Drag Prediction Workshops [12]. The NASA CRM [13] consists of a contemporary supercritical transonic wing with flow-through nacelles and a fuselage that is representative of a wide-body commercial transport aircraft. The CRM-HL is also an open geometry

that was used in the AIAA Geometry and Mesh Generation Workshop [14] and the Third AIAA High-Lift Prediction Workshop [15].

Wind-tunnel tests of the CRM-HL were carried out in the NASA Langley Research Center (LaRC) 14- by 22-foot Subsonic Tunnel (14×22) in fiscal year 2021 [16]. The primary goal of the tests was to demonstrate the effectiveness of slat noise reduction concepts, such as the SGF, at a technology readiness level (TRL) near 5, which is higher than previous tests [17], [18]. Computational fluid dynamics (CFD) and computational aeroacoustics calculations using the CRM-HL geometry were used to prescribe suitable SGF geometry for the airframe. Previous SGF structural design and analysis work [9] was extended to the CRM-HL in 2D and 3D to develop structural implementations that represent functioning flight hardware. Those structural implementations were then scaled to the 10% CRM-HL wind-tunnel model and simplified to be nonarticulating but retained boundary conditions, dimensions, and materials to meet the requirements for dynamic scaling. Accordingly, SGF treatment integration features were designed into the wind-tunnel model. All dimensions were at 10% scale (including thicknesses), and nitinol (NiTi) material was used for the treatments.

Dynamic scaling of the SGF treatment to the CRM-HL for testing in the 14x22 wind tunnel was done to assess the impact of treatment dynamics on aeroacoustic performance. Risks associated with testing the dynamically scaled components were mitigated in the wind-tunnel model via details of the treatment integration into the airframe. However, coupling between the flow and elastic treatments was anticipated, with commensurate concerns of static and dynamic stability. It was recognized that incorporation of dynamically scaled components in anything but an aeroelastic test is relatively uncommon. Nonetheless, it is anticipated that developing technology for reconfigurable/adaptive/morphing aerospace structures will make studies like the 14×22 wind-tunnel test of the CRM-HL more commonplace in the future. This motivates the need for fully coupled aeroelastic stability analyses of adaptive SMA structural technologies for airframe noise reduction.

III. Technical Objective

Fluid-structure interaction (FSI), in particular aeroelastic flutter, is a concern for an SGF treatment, and the analyses in this project were used to determine whether the SGF design possessed static and dynamic aeroelastic stability. In general, FSI becomes important when a product or structure is operating in a fluid flow regime where the flow affects or excites a structural response or vice versa. In this situation, the flow and the displacement of the structure are not independent problems but are intimately tied together. As a result, a coupled solution is necessary to understand the performance of the system under fluid and mechanical loading.

Therefore, the objective of this work is the development of computational models and analysis of the coupled fluid-structure response of SGF noise treatments applied to the leading-edge-slat component of a high-lift system typical of modern transport aircraft. The technical approach involved 1) development of high-fidelity fluid and structure models for a representative subdomain of the anticipated baseline test conditions for the CRM-HL in the 14×22 wind tunnel and 2) study of the coupled fluid-structure response of the dynamically scaled SGF. The response included the quasi-static aeroelastic deformation and the dynamic stability. An initial aeroelastic exploration of the SGF response was performed using a 2D model, followed by an aeroelastic assessment of a 3D SGF structure.

The conditions of interest correspond to the approach and landing phases of flight: nominally Mach 0.2 at sea level with an angle of attack of 8°. The SGF designs were assessed for static aeroelastic deflection as well as dynamic aeroelastic stability. Acceptable response characteristics are necessary for similar treatments to be considered practical for further study in flight tests or for implementation in a service environment.

IV. Tools and Methods

The key tools and analysis methods that were used in the FSI analyses of the SGF are described here. These tools include the CFD code (Loci/CHEM), the nonlinear computational structural dynamics (NL-CSD) code (Abaqus), the coupling tools (ATA's multiphysics engine, which uses the SIMULIA Co-Simulation Engine [CSE]), and the partial Floquet stability analysis technique. The general stability analysis procedure consisted of the following steps:

1. Perform a rigid CFD simulation to establish initial flow conditions.
2. Perform a quasi-static cosimulation to determine the static equilibrium state. The CFD simulation part of the cosimulation was restarted from the converged, rigid simulation.
3. Perform a dynamic or time-accurate cosimulation in which the CFD and NL-CSD codes use the same time step and communicate in lockstep. The dynamic cosimulation was restarted from the quasi-static solution and perturbed using impulsive load applied to the structure.
4. Perform system identification to estimate aeroelastic damping and frequencies. Structural responses—in this case, displacements—from key locations are used as input to the partial Floquet method to assess stability.

A. Overview of the Multiphysics Framework Coupling Methodology

The FSI simulations are conducted using a loosely coupled but tightly integrated domain decomposition approach in which the governing equations of motion for each domain (the fluid domain and the solid or structural domain) are solved using approaches or methods most appropriate for that domain. The CFD solver Loci/CHEM is integrated with the NL-CSD solver Abaqus in a fully coupled, FSI form. The coupling of the CFD and NL-CSD solvers is done using SIMULIA's Co-Simulation Engine (CSE), which is a software infrastructure that enables cosimulation and consists of a runtime environment that synchronizes the applications, coordinates communication, and provides spatial and temporal mapping at the domain interface [19], [20].

In a domain-decomposition approach to a coupled aeroelastic interaction problem, the CFD code will compute the traction ($\vec{T}_w$) (or force, $\vec{F}_w$) vector at the fluid-structure interface (or wetted surface), and the NL-CSD code will compute the resulting structural displacements ($\vec{x}_w$) due to those loads. The overall procedure for a typical problem is illustrated in Fig. 2.

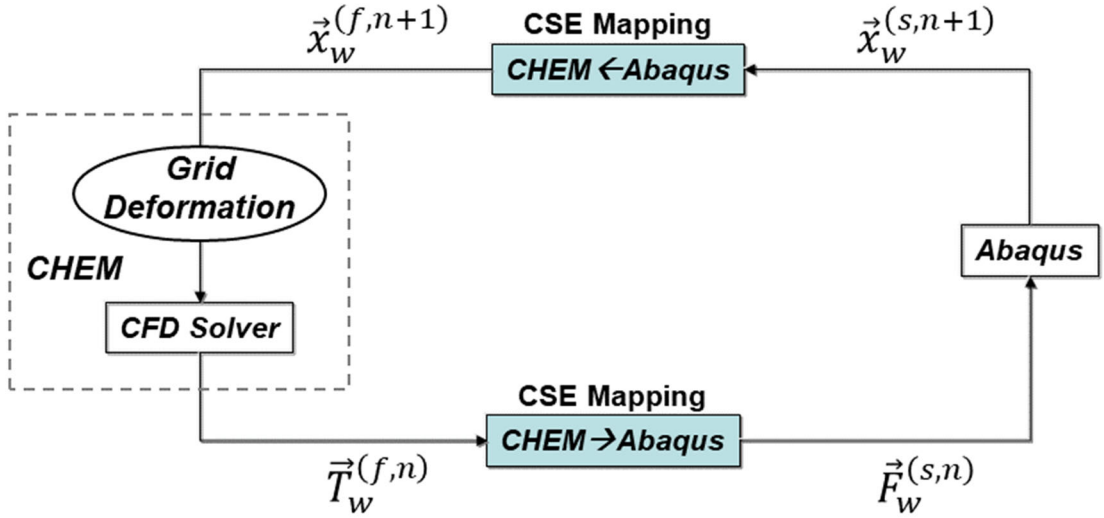

Fig. 2 Fluid-structure cosimulation data-mapping procedure.

Since a domain-decomposition approach is utilized, each domain will be suitably discretized for the appropriate solver. As such, the interface between the two domains will almost certainly be discretized differently and will not match. The data transfer at the wetted surface interface is done using the mapping tools provided by the CSE. Once the CFD wetted surface is moved to conform to the structural deformations, the flow solver adapts the volume grid to reflect these changes [21].

For temporal coupling (i.e., the frequency at which the two solvers exchange data), the CSE supports multiple options, including first order, higher order, and subcycling. The first-order data coupling option exchanges data once per time step and thus reduces the temporal order of accuracy of the coupled solution to at most first order, regardless of the temporal accuracy applied to the constituent codes. Data are exchanged upon completion of full time steps within the codes, and the codes may employ unequal numbers of subiterations to get to the next time step. The higher-order coupling option exchanges data multiple times per time step and utilizes subiteration convergence to ensure that consistent data are shared between codes. This convergence removes the lag error of the first-order schemes, and ultimately the order of accuracy of the coupled solution will be that of the lowest temporal accuracy of the constituent codes. As Loci/CHEM and Abaqus are both at most second-order accurate, second-order temporal accuracy is the most that can be attained in this application. In the subcycling coupling option, multiple time steps can be taken per data exchange. This option requires that the constituent codes line up at integer values of time steps, although the number of time steps each code takes before data exchange need not be the same. This option may be appropriate when considering problems with disparate time scales (e.g., when the fluid response is much faster than the structural response), and it mitigates the computational expense of running Abaqus in lockstep with Loci/CHEM.

In previous work, the computational framework discussed above was applied to validation problems of static and dynamic aeroelasticity in high subsonic and mildly supersonic flows [20] and to a hypersonic aerothermoelastic case [22]. Additionally, the techniques have been applied to supersonic nozzle flows to estimate the side loads on the nozzle of the Space Shuttle main engine [23] and to assess the stability of the landing gear door for a business jet [24].

B. Loci/CHEM

The CFD solver used in this work is Loci/CHEM, which is a modern multiphysics simulation code that is capable of modeling chemically reacting multiphase high- and low-speed flows. Loci/CHEM, which was developed at Mississippi State University, is written in the Loci framework and is a Reynolds-averaged Navier-Stokes (RANS) finite-volume flow solver with a cell-centered control volume definition for generalized or arbitrary polyhedrals [25]. It uses density-based algorithms and employs high-resolution approximate Riemann solvers to solve finite-rate chemically reacting viscous turbulent flows [26]. Loci/CHEM contains a robust grid deformation capability that allows it to morph the high-aspect-ratio cells common in viscous flow simulations to resolve boundary layers without sacrificing cell quality [21]. Loci/CHEM has several features and capabilities that make it well suited for FSI cosimulations at a reduced computational expense and increased robustness. These FSI cosimulations are described in the following subsections.

1. Subdomain Extraction

The majority of the computational expense in the coupled simulations is due to the high cost of CFD simulation. This expense can be lowered by reducing the size of the computational domain using the `vogcut` (volume grid cutting) utility. The `vogcut` utility extracts a subset of cells from a larger volume mesh, enabling the extracted mesh to be run as a local subdomain model, reducing the computational cost. The subsets to be extracted can be defined with simple geometric shapes (e.g., box, sphere, and cone), and all cells with their cell center inside the defined shape will be extracted.

2. Boundary Condition Interpolation and Scaling

Loci/CHEM has a boundary condition interpolation feature known as `scalablePrescribed`. This feature allows the flow solution from a completed simulation using one mesh to be interpolated onto a second mesh for use with boundary condition specification and/or flow initialization. This feature works by interpolating the solution from one cloud of points representing the first mesh to a second cloud of points representing the second mesh. It may be used for cases where the second mesh is a subset of the first, like when `vogcut` is used to generate the second mesh, or for cases where the two meshes are entirely dissimilar. This capability is applicable to both inflow and outflow boundary conditions, and only the solution data required for the respective boundary condition are used.

During simulation, Loci/CHEM generates solution files, referred to as `put` files, with the variable information (pressure, velocity, temperature, turbulent kinetic energy, turbulent eddy viscosity, and species mass fractions) located at the cell centers of the CFD mesh. These files can be used to initialize a subsequent simulation and/or to provide boundary conditions via the `scalablePrescribed` functionality. The `scalePut` utility[7] allows the user to scale any of the variables in the `put` file by a user-defined amount. This utility can be used to scale the pressure of a flow solution while keeping the Reynolds and Mach numbers constant, which saves CPU time because the `put` file can be instantly scaled to the alternative pressure condition without the need to rerun the analysis. As long as these dimensionless numbers are held constant, the character of the flow remains the same, and the scaling approach is valid. The pressure coefficient over the CRM-HL wing section for a range of dynamic pressure cases is shown in Fig. 3. The pressure coefficient distribution is roughly the same for all cases because of dynamic similarity.

[7] ATA Engineering, https://github.com/ATAEngineering/scalePut.

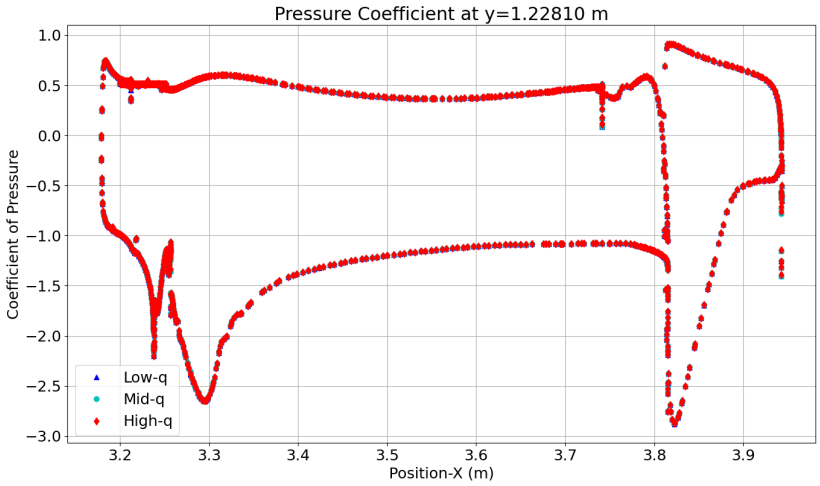

Fig. 3 Pressure coefficient for three different flow conditions.

3. Cell Quality Remediation

Poor-quality cells can hinder or inhibit solution convergence. This can be the case even when the regions of poor quality are localized to a small number of cells and do not affect global quantities of interest such as pressure coefficient or skin friction. As part of the flux calculation for each cell face in the mesh, solution values at cell faces must be reconstructed from solution values at cell centers (since Loci/CHEM is a cell-centered finite-volume code). To achieve second-order spatial accuracy, a first-order reconstruction is used. However, Loci/CHEM will by default use a more robust, but less accurate, zeroth-order reconstruction in regions of poor cell quality. This zeroth-order reconstruction results in locally first-order spatial accuracy. Loci/CHEM determines that cells with a volume ratio greater than 50 or a maximum included angle greater than 150° constitute poor-quality regions. If the region of poor cell quality is small, this local change can have a negligible effect on solution accuracy while greatly helping robustness.

The `cellQualityRemediation` module[8] extends this functionality in Loci/CHEM by allowing the user to decrease the volume ratio and maximum included angle thresholds from their default values, thereby designating more cells as being of poor quality. It also allows the user to include all cells adjacent to those flagged by the volume ratio and maximum angle thresholds in the poor-quality-cell region. This module was utilized for the 3D SGF aeroelastic assessment in section VI.

C. Stability Analysis

Aeroelastic stability is determined by analysis of the time-domain responses after the system has undergone a perturbation designed to excite the modes of interest. A system with positive damping will dissipate energy and return to a near-static-equilibrium configuration, whereas a system with negative effective damping due to aerodynamic forcing will exhibit an initial exponential growth in the response amplitude. Obviously, exponential growth cannot be sustained in nature, and in physical systems, this condition ultimately results in the failure of the structure or the presence of a limit cycle oscillation.

In the simplest form, the stability of the system may be assessed by visually inspecting the response and determining whether the response envelope grows or decays in time. Growth identified by this simple inspection indicates an instability, and decay represents positive stability. Unfortunately, visual inspection is able to determine stability only as a binary state: either the system is stable or it is not; it is not able to characterize the degree of an instability (i.e., quantify damping), and it is not able to ascertain the extent to which individual structural modes contribute to stability. Additionally, when the response is complicated, with appreciable contribution from many structural modes, an accurate visual inspection may require lengthy simulation time to observe adequate growth or decay in the response, leading to excessive computational expense.

Quantitative assessments of stability that provide estimates of component frequencies and damping values are possible through a variety of computational methods (e.g., Prony's method, the eigenvalue realization algorithm

[8] ATA Engineering, https://github.com/ATAEngineering/cellQualityRemediation.

[ERA], fast Fourier transform [FFT]-based methods, and partial Floquet). Partial Floquet [27] was developed for the more complex case of linear time-periodic systems but works equally well in analysis of linear time-independent systems and was therefore selected to provide the quantitative stability assessments here due to our extensive familiarity with the methodology.

One challenge with quantitative stability assessment occurs when the structural stiffness is variable, as can occur with nonlinear material properties. This challenge is particularly relevant to SMAs, where modal frequencies are notoriously a function of deformations. To better understand how variable stiffness may affect stability results, a simple ordinary differential equation (ODE) with a mild nonlinearity is considered:

$$\frac{\partial^2 y}{\partial t^2} + 2\omega(t)\zeta\frac{\partial y}{\partial t} + \omega^2(t)y = 0 \tag{1}$$

$$\omega(t) \equiv 2\pi\left(\Omega_{base} + \Omega_{vary}y\right) \tag{2}$$

An example of the above ODE with a base frequency of 1084 Hz, a varying nonlinear component of 100 Hz/unit, and a damping ratio of 0.1% is provided in Fig. 4.

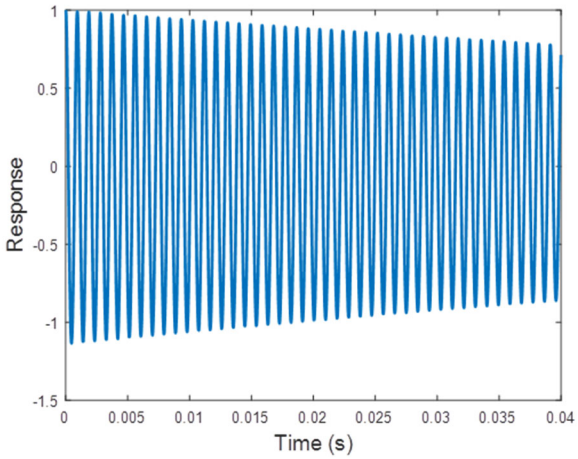

Fig. 4 Example of response with mild frequency nonlinearity.

Table 1 provides the identified results if three modes are extracted. Two frequencies are identified in the region of the base frequency—one with positive stability and the other with negative stability and neither at the prescribed 0.1% damping ratio. Despite the detected "instability" with a damping ratio of −0.12%, it is evident from visual inspection that this simple ODE is stable. Additionally, the harmonic appears at the correct damping ratio; however, the harmonic is expected to be at a much lower energy level and may not be detected if other modes are present. The takeaway from this simple example is that if a mode with variable frequency is detected as multiple frequencies, the damping ratios require careful inspection to assess their accuracy.

Table 1 Partial Floquet results for three modes.

(Detected Frequency)/(Base Frequency)	Damping Ratio
1.9802	0.10%
0.9934	−0.12%
0.9871	0.51%

V. 2D SGF Aeroelastic Exploration

As previously mentioned, the SGF must be assessed for static aeroelastic deflection as well as for dynamic aeroelastic stability. In order to bound the SGF stability estimates, an aeroelastic parameter study was performed using a 2D model. These 2D analyses were then used as a pathfinder for the 3D analyses described in the next section.

A. Description of Models

The 2D unstructured, viscous mesh contained 350,955 nodes and 697,151 elements. The 2D SGF finite element model (FEM) includes the slat, the main wing, and the SGF technology element. The SGF is modeled using general-purpose shell elements, and the slat and main wing are assumed rigid and are represented using rigid body elements.

The first step in setting up FSI simulations is to define the wetted surface where the fluid and structure exchange information. Physically, the wetted surface represents the location where the fluid and structure interact. The CFD wetted surface definition includes surfaces on both the SGF outer mold line (OML) and the inner mold line (IML). The SGF FEM is defined using general-purpose shell elements with the nodes located on the OML. However, the shell elements can only be loaded on a single side. Thus, only the CFD loading computed on either the OML or the IML can be applied. A virtual surface was defined on the IML to transfer the loads and displacements on the interior side of the SGF. The geometry for the virtual IML surface was generated by creating a spline using the IML points from the CFD surface mesh, thus ensuring consistent geometry between the CFD model and the FEM. The FEM nodes (on the OML) were projected to the spline to create nodes on the IML, thus creating a one-to-one spatial correspondence between nodes on the OML and the IML that enabled a direct node-to-node connection between the two surfaces. The virtual IML wetted surface elements were defined using elements (Abaqus `SFM3D4` elements) that have no mass or stiffness associated with them. As such, these elements are nonstructural and are used only to transfer the wetted surface loads and displacements. Therefore, to connect the IML elements to the structural elements on the OML, the IML nodes were rigidly connected to the OML nodes.

The addition of the IML virtual wetted surface was verified to not change the structural response of the SGF FEM via a series of numerical tests. The first test applied a uniform unit pressure load to the original FEM and to the modified FEM with the IML wetted surface, and the displacements were compared. The maximum difference in the horizontal component of displacement was 1%, with the difference of most nodes being on the order of 0.2%. The maximum difference in the vertical component was 0.8%, with the difference of most nodes being on the order of 0.1%. The second test involved comparing the eigensolution for the baseline and modified SGF FEMs. There was less than a 0.9% difference in the natural frequency of the first four modes and less than a 0.01% difference in the total mass. Due to the small differences between the two FEMs for the static response and eigensolutions, it was clear that the virtual IML wetted surface had very little impact on the structural response of the SGF FEM.

B. Results

An aeroelastic parameter study was performed to bound the SGF stability estimates. Five different aeroelastic simulations were performed in which both fluid and structural properties were varied. The Mach number was held constant at 0.2, and the dynamic pressure was varied from one-quarter of the nominal value (nominal q = 2884.8 Pa) to six times the nominal value. The dynamic pressure was increased by increasing the fluid density and pressure while keeping the velocity and temperature constant. This approach has the effect of keeping the Mach number fixed and not changing the fluid compressibility effects while increasing the dynamic pressure.

In addition to changing the aerodynamic parameters, the stiffness of the SGF was also varied to produce a 50% increase and 50% decrease in the first natural frequency (the natural frequency of the first mode having nominal stiffness is 4,206 Hz). The stiffness was decreased by decreasing the modulus, and the stiffness was increased by increasing the thickness.

1. Rigid Flow-Field Comparison

The nominal approach condition for the CRM-HL test was Mach 0.2, but a study was performed to examine the effect of increasing Mach number on the local flow around the SGF technology element. Selected velocity vectors and Mach number contours in the region between the slat and the main wing are shown in Fig. 5.

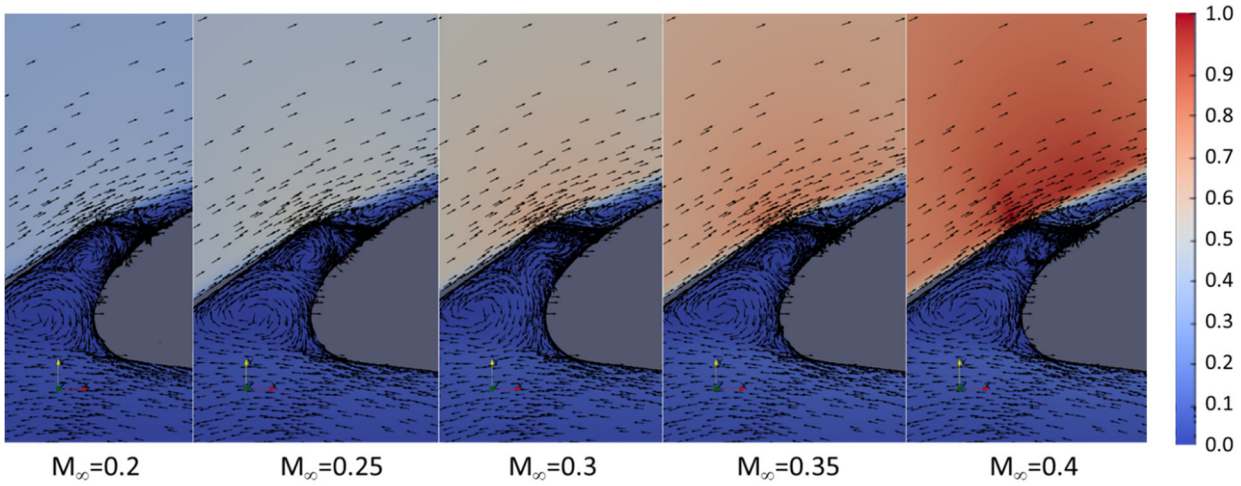

Fig. 5 Rigid flow solutions for different Mach numbers, with velocity vectors superimposed.

2. Quasi-static Aeroelastic Cosimulation

For the quasi-static cosimulations, the time integration mode in Loci/CHEM was set to steady state, and the Abaqus `*DYNAMIC, APPLICATION=QUASI-STATIC` solution procedure was used. The subcycling temporal coupling option was used, and the cosimulation converged in fewer than fifty data exchanges. On the flexible SGF surfaces, Loci/CHEM imports displacement from Abaqus and exports nodal force to Abaqus. The quasi-static aeroelastic deformation of the SGF with increasing free-stream dynamic pressure is shown in Fig. 6. As expected, the deformation increases with increasing dynamic pressure, but due to the nonlinear geometric effects, the increase in displacement is not linearly proportional to dynamic pressure. The location of the maximum deflection occurs at approximately the midchord location (node 801) and shifts slightly aft (node 800) as the deflection further increases. A summary comparison of the quasi-static analyses is provided in Fig. 7, where the magnitude has been nondimensionalized by the SGF thickness. The displacement includes visible nonlinear behavior due to the large displacement geometric effects that occur at the higher dynamic pressure conditions; at the highest loading condition, the displacement is approximately 4.5 times the thickness. Using the decreased modulus, the displacement is 3.3 times larger compared to the nominal modulus. Increasing the thickness to 0.003″ decreases the response by a factor of 4.23 compared to the response using the nominal 0.002″ thickness.

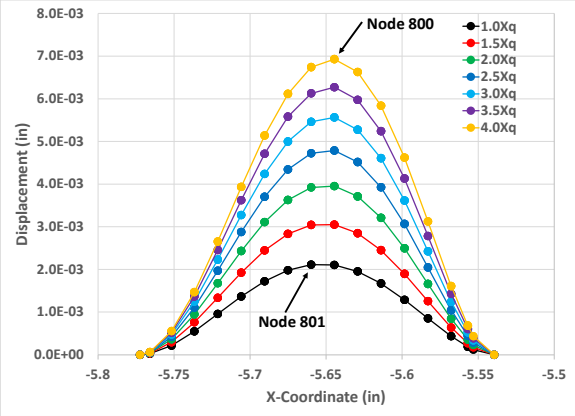

Fig. 6 The quasi-static displacement of the 2D SGF increases with dynamic pressure.

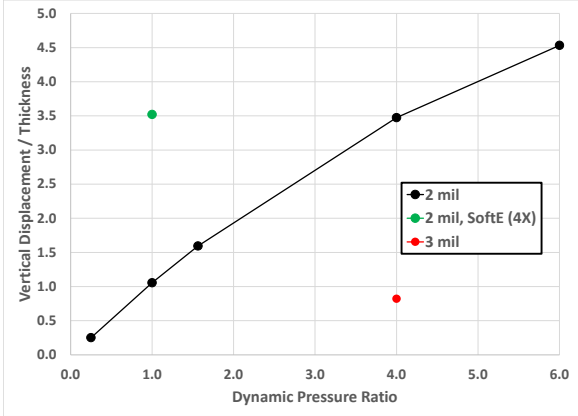

Fig. 7 Quasi-static displacement summary, node 801.

3. *Dynamic Aeroelastic Cosimulation*

The quasi-static aeroelastic analyses serve as the initial conditions for the dynamic cosimulations, which were performed to assess the 2D SGF dynamic stability. A dynamic simulation was performed using the Abaqus/Implicit solver and the Loci/CHEM solver running in time-accurate mode. Both solvers used the same time step, $\Delta t = 1.25 \times 10^{-6}$ s, and the two solvers exchanged data ten times per time step using the higher-order data exchange scheme. The time step was based on resolving the first natural frequency, and a temporal resolution study was performed with time steps corresponding to 100, 200, and 400 points per period; a temporal resolution of 200 points per period was deemed sufficient. In addition to the time-step-resolution study, subiteration convergence studies were performed using 6, 10, and 20 subiterations; a value of 10 subiterations was found to be sufficient.

The dynamic cosimulation was restarted from the quasi-static solution and perturbed using an impulsive load applied to the structure. The impulse function was of short duration, $20 \times \Delta t$, such that it had minimal interaction with the mean flow. Given the temporal nature of the impulsive load, all the modes were excited, but the spatial definition was similar to the fundamental mode shape and designed to excite mode 1. The transient response of node 801 is plotted in Fig. 8 for the various cases conducted for the aeroelastic stability parameter study. The response for the sixfold increase in dynamic pressure and nominal SGF thickness was qualitatively similar to the four-times dynamic pressure case and is not shown. The response at the nominal dynamic pressure, Fig. 8(a), shows that the oscillations occur about the static equilibrium condition. At the fourfold increase in dynamic pressure, Fig. 8(b), the vibratory response initially occurs about the original equilibrium but then shifts to the response about another equilibrium state. This trend is also observed when the thickness is increased to 0.003″, as shown in Fig. 8(c). The softened modulus case, Fig. 8(d), exhibits a dramatically different response. Initially it follows the same trend as the nominal stiffness case, but after thirty periods of oscillation, it begins to respond in a limit cycle oscillation (LCO) state.

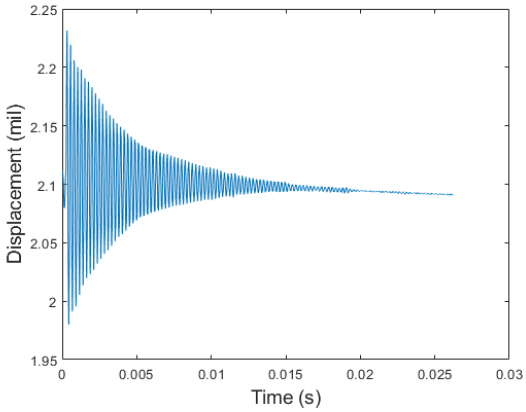

(a) Nominal q, nominal thickness

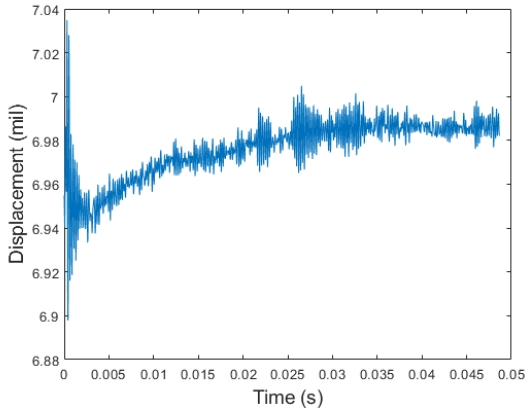

(b) 4× q, nominal thickness

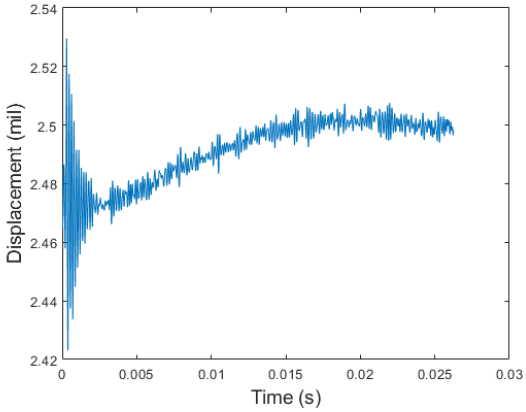

(c) 4× q, 3 mil thickness

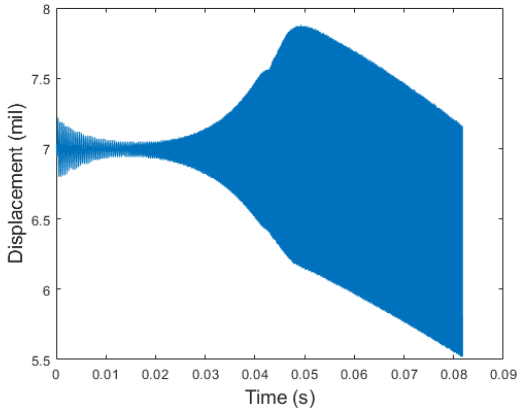

(d) Nominal q, nominal thickness, decreased E.

Fig. 8 2D SGF dynamic node 801 responses.

The rapid decay at the nominal dynamic pressure is clearly evident in Fig. 8(a) and from visual observation can be determined to be stable. The response at the higher-dynamic-pressure conditions is considerably more complex and makes visual inspection of stability more difficult; stability was ascertained using the partial Floquet system identification described in section IV.CI. Before the system identification technique could be applied, the response signal was detrended. The nominal-dynamic-pressure, nominal-stiffness, and higher-dynamic-pressure cases used the entire signal, whereas the softened modulus case that exhibits an LCO response used the last forty to fifty periods of the signal. All cases were identified as stable.

VI. 3D SGF Aeroelastic Assessment

This section summarizes the full 3D aeroelastic analysis that was performed.

A. Description of Models

CFD and NL-CSD semispan models for the CRM-HL geometry were created in Loci/CHEM and Abaqus. The models were used to evaluate the dynamic stability of the SGF under the two flow conditions shown in Table 2. The baseline condition corresponds to a nominal landing condition, and the high-q case corresponds to a landing condition in which there is a wind gust increasing the dynamic pressure. The dynamic pressure of the high-q case was chosen to nominally result in a deformation equal to four panel thicknesses using an estimated pressure differential between the pressure and suction sides of the SGF and assuming a uniform pressure distribution.

Table 2 Flow conditions for SGF aeroelastic assessment.

Case Name	Dynamic Pressure (Pa)	Mach	Reynolds Number (m^{-1})	Angle of Attack
Baseline	2873.10	0.2	4.6×10^6	8°
High-q	5390.49	0.2	4.6×10^6	8°

An overview of the cosimulation setup is presented in Fig. 9. The NL-CSD model cosimulates with a subdomain CFD model that is informed by a vehicle-level semispan rigid CFD solution. The semispan model is run a priori and is used to supply the subdomain model with initial conditions and boundary conditions. The subdomain CFD and NL-CSD models are run concurrently during the cosimulation.

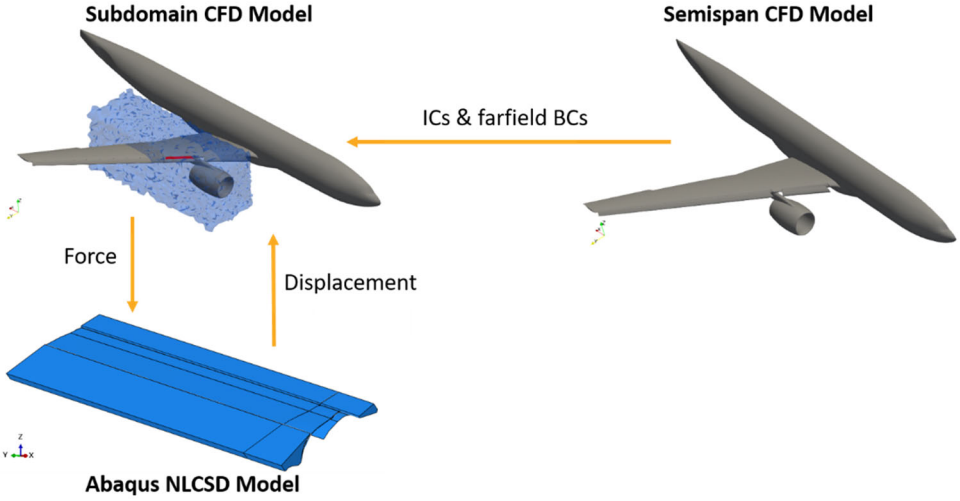

Fig. 9 Cosimulation setup with semispan/subdomain CFD models and NL-CSD FEM.

1. Vehicle Semispan Flow-Field CFD Computation

The CRM-HL semispan model was used to conduct a RANS CFD simulation at the baseline flow conditions using the Spalart-Allmaras turbulence model. The detailed geometry of the CRM-HL model, with its myriad small edges

and features, made generating a high-quality unstructured CFD mesh challenging. The small edges and features led to a collapse of the prismatic layers generated off the vehicle body during the meshing process. This situation in turn resulted in large volume ratios at the interface between the anisotropic prismatic layers and the isotropic core mesh, which resulted in stability problems for Loci/CHEM. To alleviate this problem, the `cellQualityRemediation` module (described in section IV.B.3) was used. In general, the regions of poor cell quality comprise a very small number (<< 1%) of cells compared to the total number of cells in the domain. Furthermore, it was demonstrated that the local reduction in spatial order of accuracy has a negligible effect on the key outputs of the simulation (e.g., pressure coefficient and skin friction coefficient on the vehicle body).

The pressure and skin friction coefficients on the wing surface were compared to the mean flow field of a previous scale-resolving CFD solution obtained by NASA using PowerFLOW, as shown in Fig. 10. Qualitatively, the results showed good agreement and demonstrated Loci/CHEM's ability to accurately model the highly separated flow near the wing-nacelle junction.

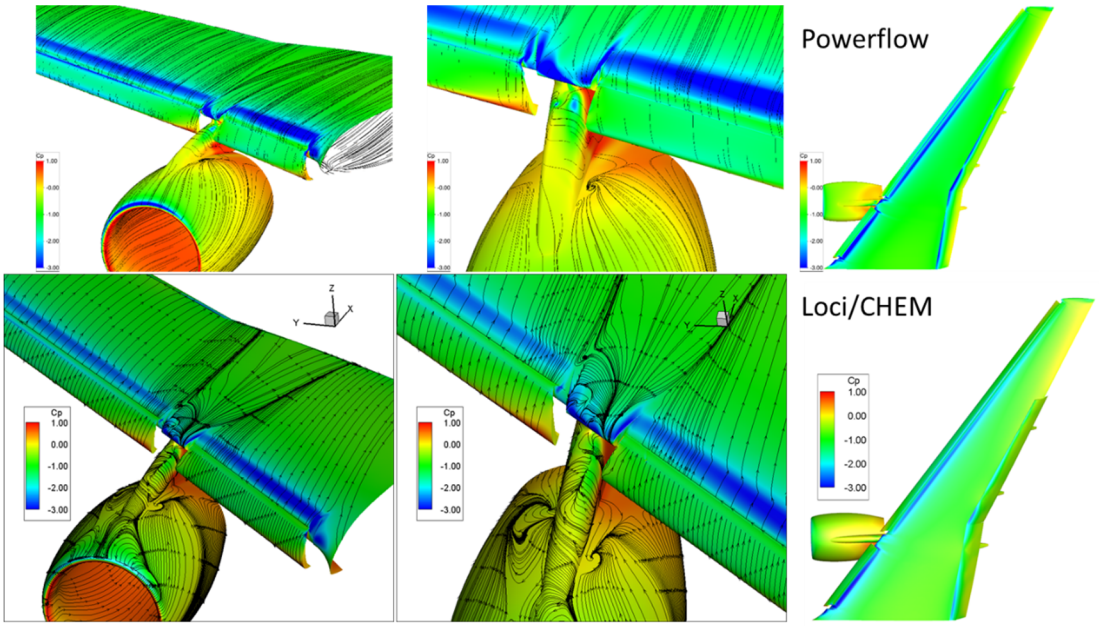

Fig. 10 Pressure and skin friction coefficient comparison between Loci/CHEM and PowerFLOW.

2. Subdomain Breakout CFD Model Creation

The CRM-HL semispan mesh was unsuitable for FSI simulation because (1) its mesh quality near the SGF was not sufficient to support large deformations (on the order of four panel thicknesses) and (2) its large size would lead to high computational expense. In an effort to improve the local cell quality to support large mesh deformations, a structured mesh was created around the flexible portion of the SGF. The structured mesh interfaced to an unstructured mesh that covered the rest of the domain. To allow each mesh region to have the highest quality cells possible, the interface at the structured/unstructured boundary was not point-matched; during simulation, Loci/CHEM interpolates the solution across the interface.

To reduce the cell count and minimize the computational expense, the subdomain modeling approach was used. For the SGF application, Loci/CHEM's `vogcut` utility was used to extract all cells that have nodes within a box defined around the flexible portion of the SGF. The subdomain, shown in Fig. 11, reduces the total number of cells by a factor of about three.

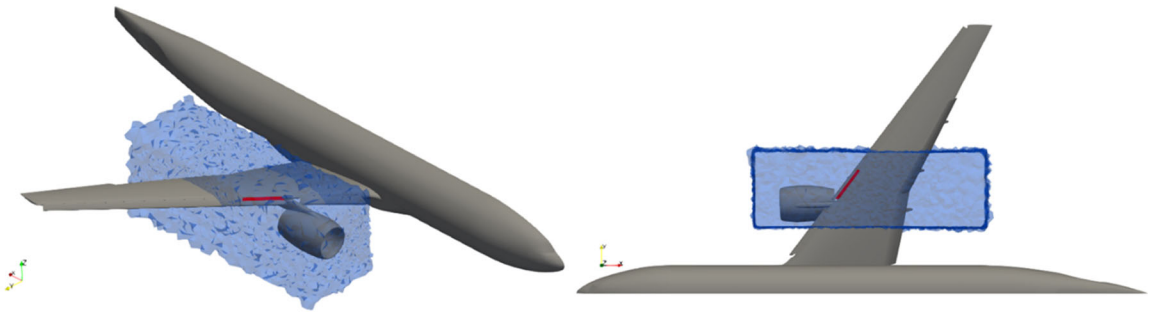

Fig. 11 Flexible SGF region (red) and the CFD subdomain around it (blue).

To ensure that the subdomain model was accurately modeling the flow, the pressure coefficient along a spanwise section was compared between the semispan simulation and the subdomain models. The subdomain models were run with the Spalart-Allmaras turbulence model, as before, and with the k-ω shear stress transport (SST) model, which was observed to have better numerical stability for this simulation. In Fig. 12, both the Spalart-Allmaras and the k-ω SST subdomain simulations show good agreement with the semispan result. For numerical stability reasons, the k-ω SST model was chosen for the FSI simulations.

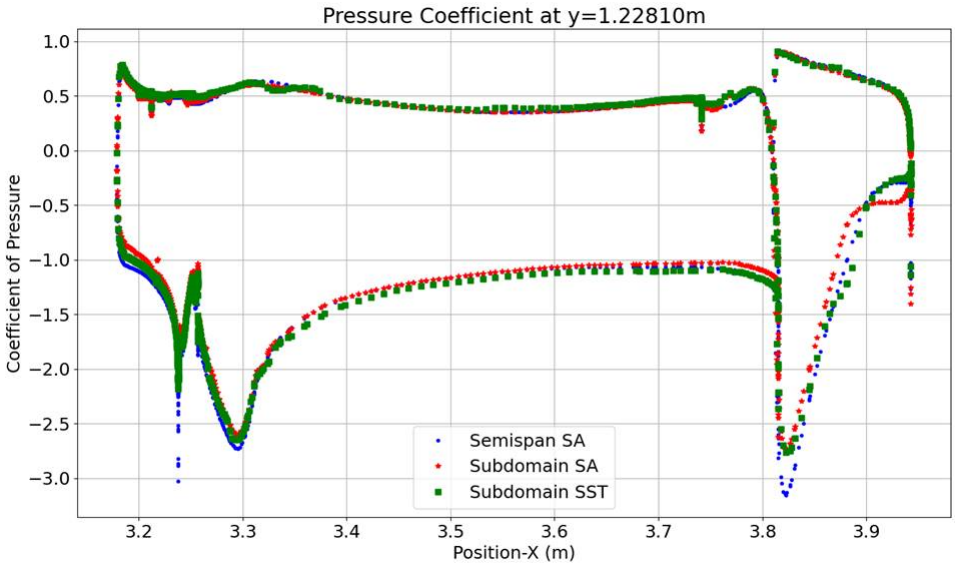

Fig. 12 Loci/CHEM subdomain simulation with SST model suggests reasonable agreement with semispan solution.

3. Nonlinear CSD Model

The fidelity of the FEM used in the FSI analysis was established to capture essential behaviors of the flexible SGF treatment to acceptable fidelity without overburdening the FSI calculation. The driving factor for simplification of the FEM stemmed from the requirement to limit the FSI computations, and thus the deformable structure, to within the boundaries of the subdomain. The computational subdomain encompasses the inboard end of the outboard slat, including the first two sections (identified as 6 and 7 for the entire model) of SGF treatment on the outboard slat component. This region was selected because of the complex flow field there, largely stemming from the presence of the nacelle and pylon, and the resulting increase in loading and unsteady phenomena around the slat and treatment components there. A CAD image showing the relevant section of the CRM-HL wing in the subdomain is shown in Fig. 13.

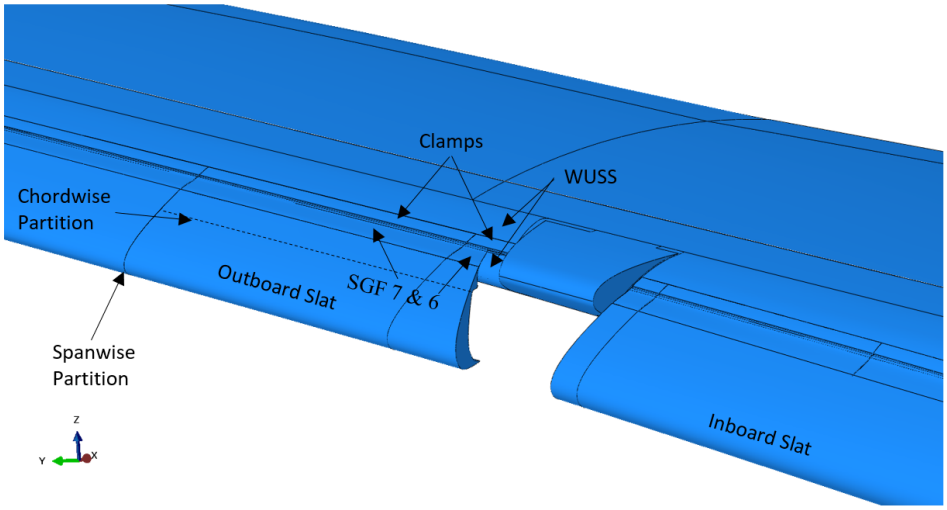

Fig. 13 CAD image of CRM-HL wing in subdomain region.

The physical model was composed of a single contiguous slat component inboard of the nacelle and pylon and another single contiguous slat component outboard of the nacelle and pylon. The subdomain approach required grid deformation to be zero at the subdomain boundaries. Although several simplifications to the slat and wing upper slat surface (WUSS) behavior were considered, the approach selected entailed partitioning the outboard slat, as shown in Fig. 13, in the spanwise direction within the outboard limit of the subdomain. The partition was taken at the outboard end of SGF section 7: the section of outboard slat within the subdomain was considered for development of the FEM, and everything outboard was neglected. The loss in mass and stiffness influence of the slat section outboard of the subdomain was recognized, and the resulting model was considered conservative from a static deflection and stability standpoint. The outboard slat section within the subdomain was further simplified by neglecting all but the trailing section, as defined by the chordwise partition near and adjoining the joint with the SGFs in Fig. 13, because it was believed that the elasticity of that section of the slat had the greatest influence on the deflection and stability of the SGF treatments. All degrees of freedom were constrained at the root end of that elastic aft section of the slat to represent its connection to the rest of the slat. The WUSS was modeled as rigid, and only the outer surface in the region of possible interaction with the SGFs was retained in the FEM. A cross-section of the model through SGF 7, showing the essential features captured in the FEM, is depicted in Fig. 14.

The physical model required fastened joints between the SGF treatment and the rest of the model for fail-safety. Limitations imposed by the small size at 10% scale forced inclusion of some features not characteristic of flight hardware, such as the ramp in the cove of the slat and the clamps on the WUSS for securement of the SGF sections, shown in Fig. 14; however, these features were deemed unimportant because they do not significantly affect the flow. It was believed that adequate fidelity could be achieved by simplifying the computational model by deleting fastener holes and introducing point-based fasteners at the relevant locations.

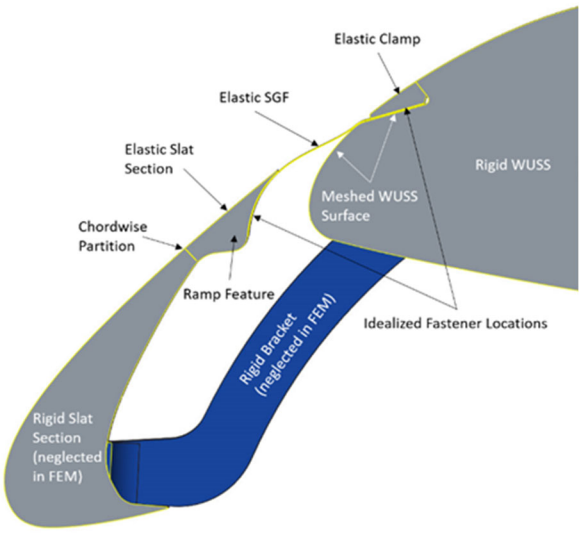

Fig. 14 Cross-section through SGF 7 showing essential features included in FEM.

Table 3. Properties of materials used in CRM-HL and FEM thereof. See Auricchio and Sacco [28] for definition of parameters.

Stainless Steel	
Property	Value
E	206.9 GPa
ν	0.26
ρ	7915 kg/m^3
Nitinol	
E_A, E_M	48.9 Gpa, 40 GPa
$\nu_A=\nu_M$	0.33
H, Transf. ε	4.40%
σ^{Ms}, σ^{Mf}	471 MPa/514 MPa
σ^{As}, σ^{Af}	196 MPa/166 MPa
Tens./Comp.	Symmetric
Ref. Temp.	24°C
$C^A=C^M$	10 MPa/K
ρ	6480 kg/m^3

The FEM resulting from the simplifications described above is shown in Fig. 15. The slat trailing section had a chord of approximately 24.94 mm (0.982″) along the outer surface at the juncture between SGF sections 6 and 7, it was meshed with linear hexahedral elements (type `C3D8R`) having an approximate global size of 1.143 mm (0.045″), and it was assigned the material properties of stainless steel listed in Table 3. Similarly, the clamps securing the aft section of the SGFs to the WUSS had a top-edge length of approximately 8.79 mm (0.346″) between SGF sections 6 and 7, it was also meshed with `C3D8R` elements having an approximate global size of 1.143 mm (0.045″), and it was assigned properties of stainless steel. The outboard edge of SGF section 6 and, similarly, the inboard edge of SGF section 7 had an unsupported length of approximately 18.26 mm (0.719″). The SGFs were meshed with continuum shell elements (type `SC8R`) having chordwise/spanwise dimensions of approximately 0.635/1.27 mm (0.025″/0.05″), and they were assigned the material properties of an SMA (nitinol) listed in Table 3. The built-in model in Abaqus for superelastic materials, which is based on the model developed by Auricchio and Sacco [28], was used to capture the large deformation behavior of the SMA.

Point-based fasteners were defined at the locations indicated in Fig. 14 to join the SGFs with the slat trailing section. Similar fasteners were defined at the relevant locations between the clamps, SGFs, and WUSS surface. A contact-tie constraint was defined between the bottom of the clamps and the top of the SGFs. Surface-to-surface contact was defined between the SGFs and the rounded nose of the clamps on top and between the SGFs and the WUSS surface below. Finally, surface-to-surface contact was defined between the tops of the SGFs and the underside of the slat trailing section.

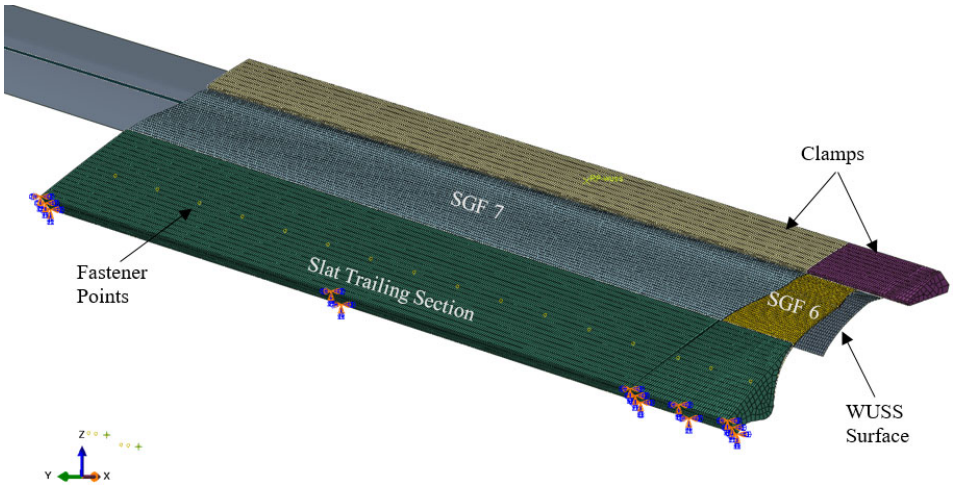

Fig. 15 FEM of simplified SGF assembly within the computational subdomain.

There were regions of the fluid domain in the vicinity of the model where it was either difficult to grid or a gap between adjacent structural components could close or open due to structural deformation during the solution. These regions correspond mainly to the interactions between the SGFs and the slat trailing section, the SGFs and the WUSS surface below, and at the inboard ends of the aforementioned regions. These regions are highlighted in Fig. 16. Virtual surfaces were created in these areas, they were meshed with surface elements, and the meshed surfaces were tied along their edges to the adjacent structures to provide a deforming-but-ever-present boundary for the fluid domain. Steady pressure loads were defined between the SGF sections and the adjacent slat trailing section with the magnitude and spanwise distribution dictated by the steady pressure distribution at the trailing edge of the slat from the steady, semi-span CFD solution. Steady pressure distributions were similarly defined between the SGF sections and the WUSS, with the magnitude and distribution again coming from the steady, semispan CFD solution. Finally, pressure loads were defined for the top and bottom surfaces of the SGF components for transfer of transient pressure loads from the CFD solver.

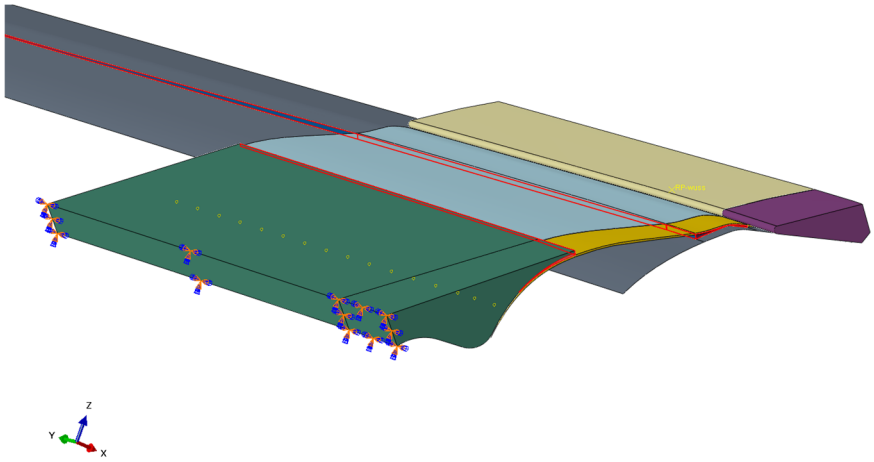

Fig. 16 FEM with virtual flow-impermeable surfaces highlighted.

The Abaqus model used in the study is depicted in Fig. 17, with monitored nodes on the two SGF sections marked with red dots.

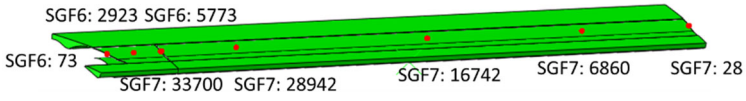

Fig. 17 Nodes monitored in Abaqus model.

B. Results

Results of quasi-static and dynamic aeroelastic cosimulations will be described in the next two sections.

1. Quasi-static Aeroelastic Cosimulation

An aeroelastic cosimulation was conducted for the baseline and high-q cases, with the goal of determining the quasi-static deformed shape of the SGF. The Loci/CHEM models were restarted from the previously generated subdomain results. As previously mentioned, the semispan solution file was used to provide boundary conditions on the sides of the subdomain box. Since the generation of the semispan solution was a computationally intensive process, the baseline solution file was scaled to generate the solution file for the high-q case using the `scalePut` utility. This scaling avoided the need to generate a new semispan solution from scratch.

The `scalePut` utility was used to scale the pressure and density by a factor of 1.9 (the ratio of the dynamic pressures between the two cases). Sutherland's law was used to calculate viscosity, and the leading coefficient in Sutherland's law (a_1, when in the form $\mu = \frac{a_1 T^{a_2}}{T+a_3}$) was scaled by the same factor. This scaling had the effect of increasing the dynamic pressure while keeping the key nondimensional parameters of the flow (Mach and Reynolds numbers) the same so that the compressibility characteristics of the flow remained unchanged.

A quasi-static cosimulation was defined using the same procedure described in the 2D SGF section. The duration of the quasi-static cosimulation was defined to be 0.1 s. The cosimulation time step, which determines how often Loci/CHEM and Abaqus exchange data, was allowed to vary over the course of the simulation as shown in Table 4. At the beginning of the simulation, the cosimulation time step was a relatively small 1×10^{-4} s. As the simulation converges toward a quasi-static state, the solutions changed less, and a larger cosimulation time step was used.

Table 4 Quasi-static cosimulation time stepping.

Simulation Time, t (s)	$0 \leq t < 0.001$	$0.001 \leq t < 0.01$	$0.01 \leq t < 0.1$
Cosimulation Time Step (s)	0.0001	0.001	0.01

To avoid large impulse forces at startup, the force passed from Loci/CHEM to Abaqus was linearly ramped from 0% at t = 0 s to 100% at t = 0.01 s. The displacements of the tracked nodes on SGF sections 6 and 7 are shown in Fig. 18 and Fig. 19. The nodal displacements are nondimensionalized by their respective panel thickness. The baseline case results in SGF section 7 displacements of slightly under two panel thicknesses, whereas the displacements for the high-q case reach three panel thicknesses.

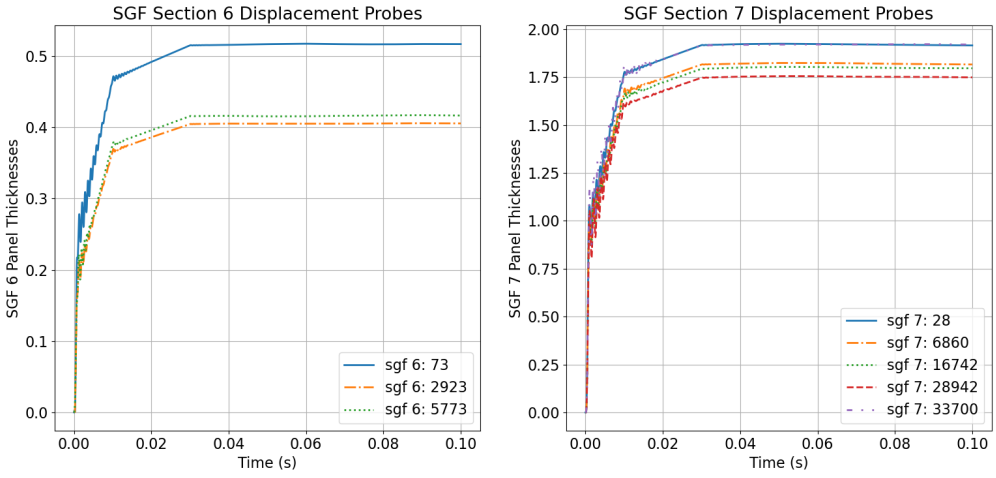

Fig. 18 Nondimensional displacement magnitude for baseline quasi-static cosimulation.

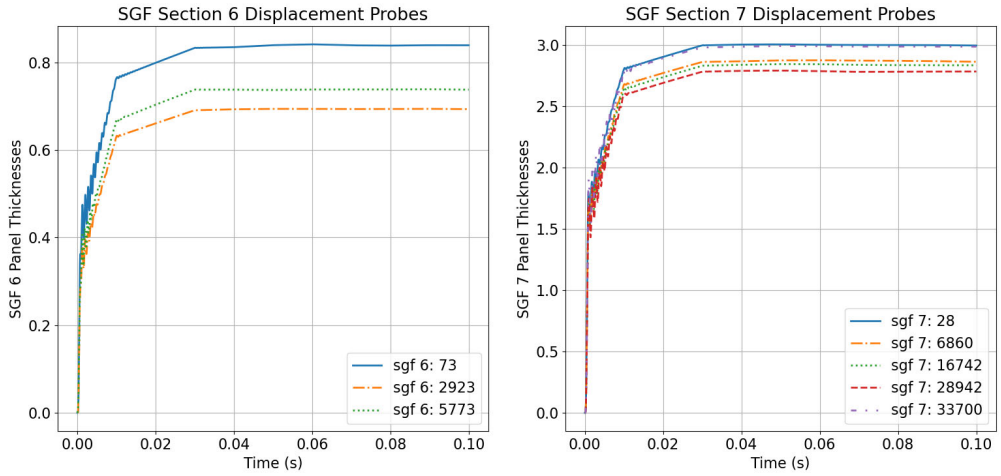

Fig. 19 Nondimensional displacement magnitude for high-q quasi-static cosimulation.

The quasi-static deformation stiffens the SGF and results in a shift of the modes to higher frequencies. The first mode for the unloaded, baseline, and high-q cases is shown in Fig. 20. The frequencies of the first ten modes versus dynamic pressure for several quasi-static loading cases is shown in Fig. 21. These results confirm that the SGF modes shift to higher frequencies with higher loading/deformation and demonstrate that the frequency spacing between sequential modes may change, which indicates that the dynamic response of the SGF will be sensitive to the deformation level.

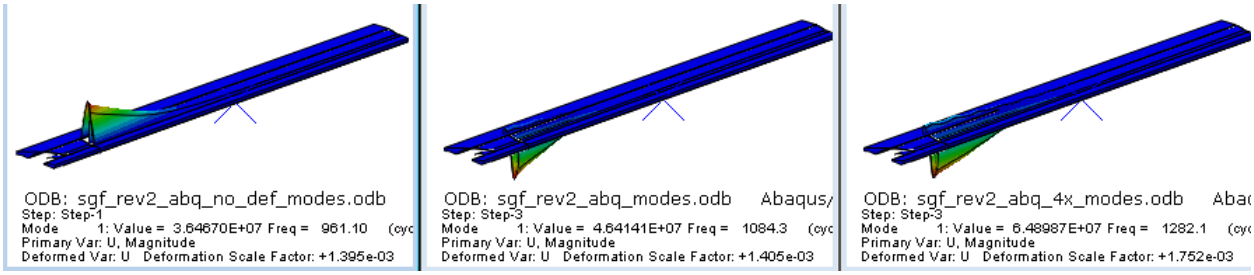

Fig. 20 Mode 1 across unloaded (left, 961 Hz), baseline (center, 1084 Hz), and high-q (right, 1282 Hz) cases.

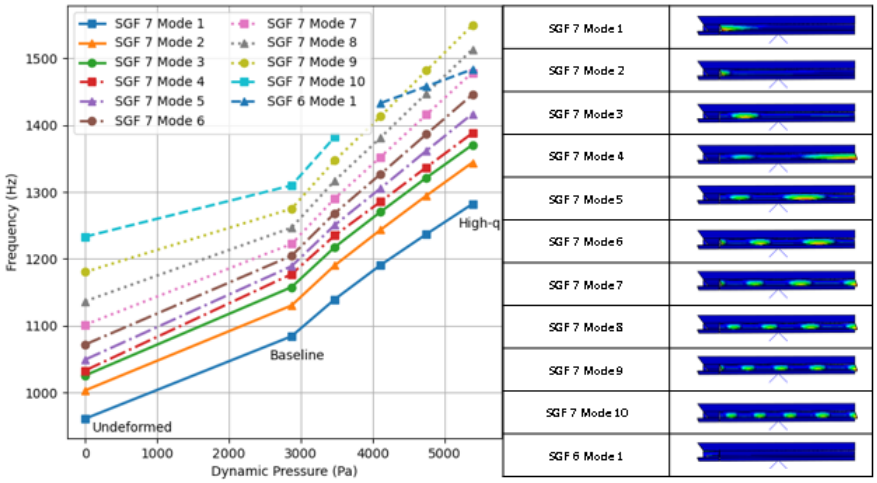

Fig. 21 Mode numbers grouped by shape (selected modes ranked by frequency on previous figures).

2. Dynamic Aeroelastic Cosimulation

Similar to the procedure used for the 2D SGF simulations, dynamic aeroelastic cosimulations were restarted from the quasi-static results with a purpose of assessing the dynamic stability of the SGF. Both Loci/CHEM and Abaqus used the same 1×10^{-5} s time step, and the cosimulation was set up to have second-order temporal accuracy with the codes communicating five times per time step (i.e., using the higher-order data exchange scheme). The SGF FEM was perturbed with a spatially distributed force that was defined as a superposition of its first four mode shapes. The force was applied as a step function at the beginning of the cosimulation, active over the initial 2.5×10^{-4} s. The magnitude of the force was small, 2.5×10^{-3} psi for the baseline case and 2.5×10^{-4} psi for the high-q case, and the purpose of the force was to excite the structure and cause it to oscillate. Stability was assessed by examining the growth or decay of the ensuing structural response. If the oscillations damped out over the course of the simulation, the SGF could be deemed stable; if they grew, it was unstable. The displacements were monitored at the same eight nodes as with the quasi-static cases. The normalized displacements on SGF sections 6 and 7 for the baseline case are shown in Fig. 22 and Fig. 23. Visual inspection indicates that the oscillations are growing smaller, but there is some evidence of a beating phenomenon, especially in the SGF section 7 results. Given the restricted length of the time history available due to computational resources, it is difficult to reach a conclusion on stability via visual inspection alone, so partial Floquet analysis was used to further assess stability.

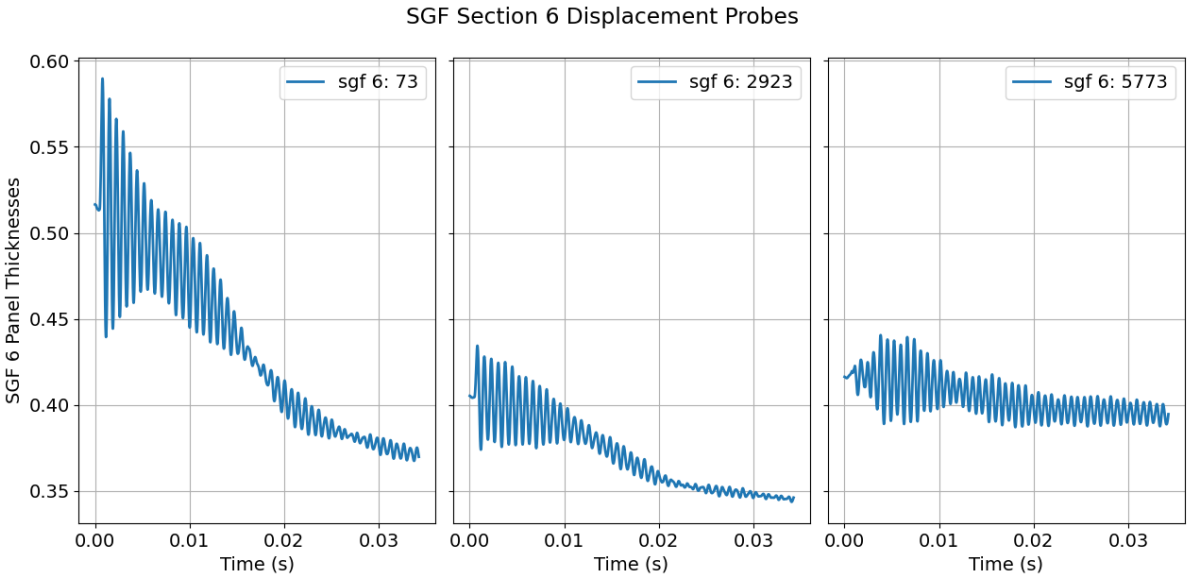

Fig. 22 Baseline dynamic pressure displacement time histories on SGF section 6.

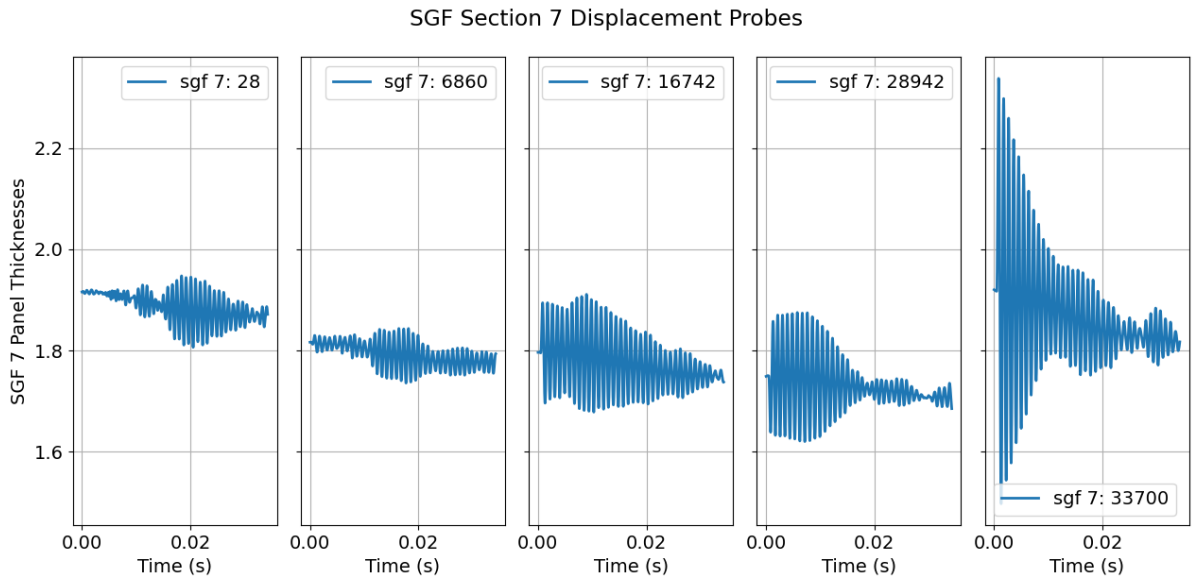

Fig. 23 Baseline dynamic pressure displacement time histories on SGF section 7.

Table 5 provides the damping ratios of the detected frequencies, obtained from a partial Floquet analysis from node 28,942 after the first 1000 time steps were discarded to avoid the initial transient around the perturbation. All frequencies detected were observed to be stable, consistent with visual inspection.

Table 5 Node 28,942 (SGF 7) baseline dynamic pressure case partial Floquet analysis suggests stable response.

Frequency (Hz)	Damping Ratio
1,070.6	0.07%
1,101.4	1.00%
1,165.5	0.007%

Note that the first two frequencies appear to correspond to the first mode (approximately 1,084 Hz at baseline deformation). This correspondence is attributed to the dependence of modal frequency on deformation (see Fig. 23). Consistent with the previous contrived example discussed in section IV.C, this dependence results in duplicate modal detections. Also similar to the example, if the duration of data from the simulation is restricted, the duplicate mode is observed to be negative. For example, if only the first 0.0422 s of the simulation is considered, the first two modes are observed as occurring at 1069.5 Hz and 1101.6 Hz with critical damping ratios of −0.26% and 0.98%, respectively. As discussed in the contrived numerical example, an identified instability can be detected even when no instability is possible due to a variable frequency response. In the above baseline dynamic pressure results, both damping ratios from the duplicate first mode are detected as stable after approximately 0.045 s.

The high-q case was run in the same manner as the baseline case. The displacement time histories for the dynamic cosimulation are shown in Fig. 24 and Fig. 25. Visually, the oscillations appear to be damping out, and there is less evidence of the beating phenomenon than in the baseline case. A partial Floquet analysis was used to confirm the assessment that the high-q case is stable. The increased dynamic pressure simulation obtained 0.0332 s of data. As expected, the DC component of the deformation is higher due to the increased dynamic pressure; however, the amplitude of deformation is noticeably less than that observed for the baseline dynamic pressure case.

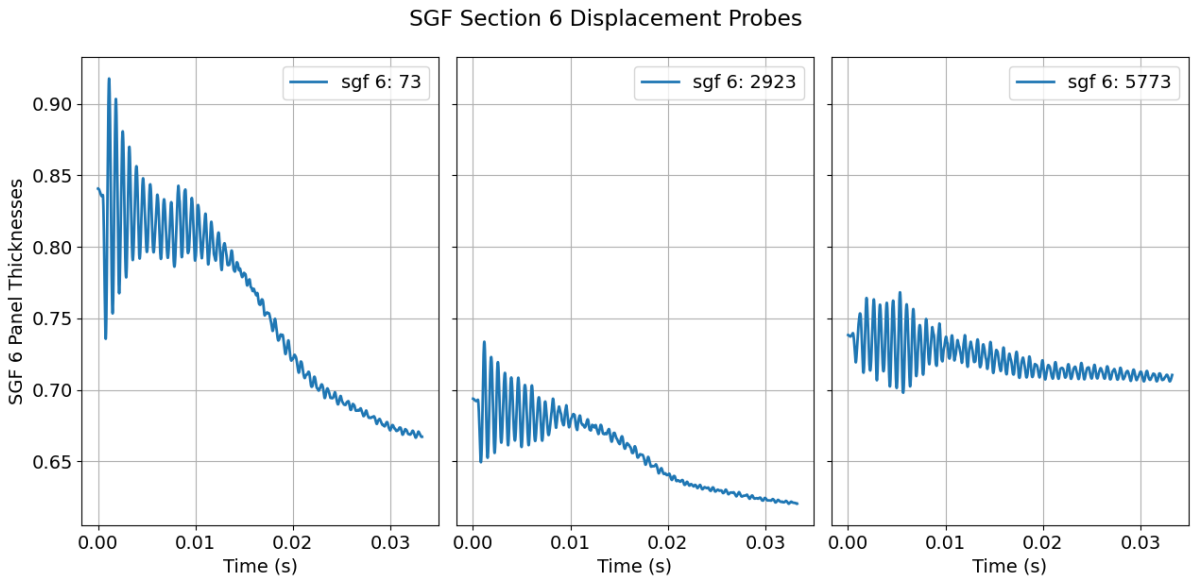

Fig. 24 Elevated (high-q) dynamic pressure displacement time histories on SGF section 6.

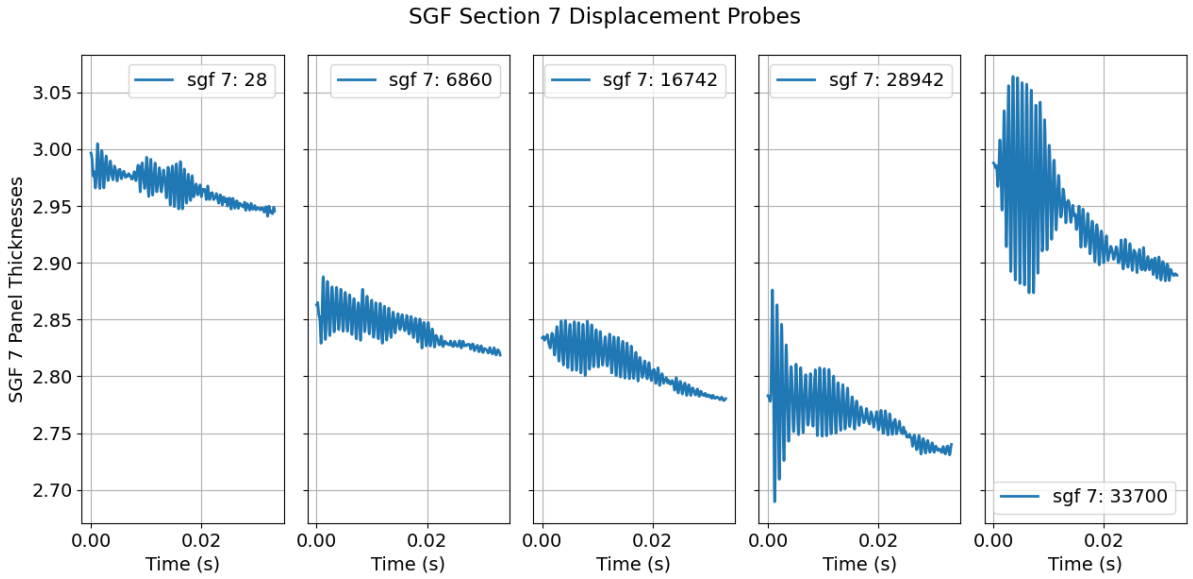

Fig. 25 Elevated (high-q) dynamic pressure displacement time histories on SGF section 7.

Table 6 provides the damping ratios of the detected frequencies, obtained from a partial Floquet analysis from node 6860 after the first 1000 time steps were discarded to avoid the initial transient around the perturbation. All frequencies detected were observed to be stable, consistent with visual inspection. The system identification technique appears to find three distinct modes in this case, and duplicate modes are not observed at the higher dynamic pressure. The distinct modal content could have a variety of causes, but it is worth noting that the system identification technique preferentially finds modes with the highest energy content first. Thus, it is possible that this case had a more even distribution of energy across the structure's modes. Another possible explanation is that the reduction in dynamic deformation as compared to the baseline case reduces frequency variations.

Table 6 SGF section 7 high-q dynamic pressure case partial Floquet analysis suggests stable response.

Frequency (Hz)	Damping Ratio
1171.8	1.75%
1268.9	1.25%
1505.0	0.85%

VII. Conclusion

Prior work on adaptive SMA SGF structures demonstrated promising slat noise reduction for aircraft in high-lift configurations. However, successful TRL maturation requires not only acoustic and quasi-static structural assessment but also aeroelastic stability analysis. This paper describes how ATA Engineering and NASA have collaborated to apply Loci/CHEM and Abaqus to solve this problem in both a quasi-static and dynamic manner. FSI analyses consisted of a 3D SGF geometry. The technical approach followed these steps:

- CFD simulation of the global flow field under the assumption of rigid geometry for a semispan model of the CRM-HL.
- Extraction or generation of a subdomain mesh in some neighborhood of the technology element. In general, the neighborhood bounds were defined to achieve a balance between accuracy and computational efficiency.
- Quasi-static cosimulation between CFD (Loci/CHEM) and NL-CSD (Abaqus) to obtain the mean deformed structural shape. A key output was the deflection of the structure, typically measured relative to panel thickness.
- Dynamic cosimulation between CFD and NL-CSD to assess aeroelastic stability. A key output of this analysis was the quantified damping from partial Floquet analysis.

Generation of suitable subdomain meshes that could also successfully be morphed on the compliant technology element boundaries required care, and specific effort was made to develop best meshing practices for the 3D SGF case due to the compliant technology element's thin structure and proximity to other rigid surfaces in the simulation domain.

Completing the technical approach also required the development of tools and methods that were not available at the start of the project:

- A cell-quality remediation module in Loci/CHEM to drop the solver to first-order spatial accuracy in regions of poor mesh quality.
- A scaling utility to simulate elevated dynamic pressures while holding the Mach and Reynolds numbers fixed.
- A force ramping capability for quasi-steady FSI to avoid large deformation overshoots that created negative-volume mesh cells upon morphing.

The long-term value of this capability is a means to substantiate margins of safety for future lightweight structures used for airframe noise reduction.

Acknowledgments

Elements of the technology described in this paper may be covered under a US Patent awarded to NASA.

References

[1] Hayes, J. A., Horne, W. C., Soderman, P. T., and Bent, P. H., "Airframe Noise Characteristics of a 4.7% Scale DC-10 Model," AIAA Paper 1997-1594, 1997.

[2] Storms, B.L., Ross, J.C., Horne, W.C., Hayes, J.A., Dougherty, R.P., Underbrink, J.R., Scharpf, D.F., and Moriarty, P.J., "An Aeroacoustic Study of an Unswept Wing with a Three-Dimensional High Lift System," NASA TM 112222, February 1998.

[3] Dobrzynski, W., Nagakura, K., Gehlhar, B., and Buschbaum, A., "Airframe Noise Studies on Wings with Deployed High-Lift Devices," AIAA Paper 1998-2337, 1998.

[4] Storms, B.L., Hayes, J.A., Moriarty, P.J., and Ross, J.C., "Aeroacoustic Measurements of Slat Noise on a Three-Dimensional High-Lift System," AIAA Paper 1999-1957, 1999.

[5] Choudhari, M.M., Lockard, D.P., Macaraeg, M.G., Singer, B.A., Streett, C.L., Neubert, G.R., Stoker, R.W., Underbrink, J.R., Berkman, M.E., Khorrami, M.R., and Sadowski, S.S., "Aeroacoustic Experiments in the Langley Low-Turbulence Pressure Tunnel," NASA TM 211432, February 2002.

[6] Mendoza, F., and Brooks, T., "Aeroacoustic Measurements of a Wing/Slat Model," AIAA Paper 2002-2604, 2002.

[7] Terracol, M., Manoha, E., and Lemoin, B., "Noise Sources Generation in a Slat Cove: Hybrid Zonal RANS/LES Simulation and Dedicated Experiment," AIAA Paper 2011-3203, 2011.

[8] Chow, L.C., Mau, K., and Remy, H., "Landing Gears and High Lift Devices Airframe Noise Research," AIAA Paper 2002-2408, 2002.
[9] Turner, T.L., and Long, D.L., "Development of a SMA-Based, Slat-Gap Filler for Airframe Noise Reduction," AIAA Paper 2015-0730, 2015.
[10] Zhang, Y., Cattafesta, L., Pascioni, K., Choudhari, M., Lockard, D., Khorrami, M., and Turner, T., "Slat Noise Control Using a Slat Gap Filler," AIAA-2020-2553, AIAA Aviation 2020 Forum, Virtual Event, June 15–19, 2020.
[11] Lacy, D.S., and Sclafani, A.J., "Development of the High Lift Common Research Model (HL-CRM): A Representative High Lift Configuration for Transonic Transports," AIAA Paper 2016-0308, 2016.
[12] AIAA Drag Prediction Workshop, URL: https://aiaa-dpw.larc.nasa.gov/ [retrieved 20 May 2021].
[13] NASA Common Research Model, URL: https://commonresearchmodel.larc.nasa.gov/ [retrieved 17 May 2021].
[14] AIAA Geometry and Mesh Generation, URL: http://www.gmgworkshop.com/ [retrieved 17 May 2021].
[15] AIAA High Lift Prediction Workshop, URL: https://hiliftpw.larc.nasa.gov/ [retrieved 20 May 2021].
[16] Lockard, D.P., Turner, T.L., Bahr, C.J., and Hutcheson, F.V., "Overview of Aeroacoustic Testing of the High-Lift Common Research Model," 2021 AIAA Aviation Forum, Virtual Event, August 2–6, 2021 (to be published).
[17] Streett, C.L., Casper, J., Lockard, D.P., Khorrami, M.R., Stoker, R., Elkoby, R., Wenneman, W., and Underbrink, J., "Aerodynamic Noise Reduction for High-Lift Devices on a Swept Wing Model," AIAA Paper 2006-0212, 2006.
[18] Horne, W.C., Burnside, N.J., Soderman, P.T., Jaeger, S.M., Reinero, B.R., James, K.D., and Arledge, T.K., "Aeroacoustic Study of a 26%-Scale Semispan Model of a Boeing 777 Wing in the NASA Ames 40- by 80-Foot Wind Tunnel," NASA TP 2004-212802, October 2004.
[19] Blades, E. L., Miskovish, R. S., Nucci, M., Shah, P., Bremner, P. G., and Luke, E. A., "Towards a Coupled Multiphysics Analysis Capability for Hypersonic Vehicle Structures," AIAA-2011-1962, 2011. doi: 10.2514/6.2011-1962.
[20] Blades, E., Miskovish, S., Luke, E., Collins, E., and Kurkchubashe, A., "Multiphysics Simulation Capability using the SIMULIA Co-Simulation Engine," AIAA-2011-3397, 2011. doi: 10.2514/6.2011-3397.
[21] Luke, E., Collins, E., and Blades, E., "A Fast Mesh Deformation Method Using Explicit Interpolation," *Journal of Computational Physics*, Vol. 231, No. 2, January 2012, pp. 586-601. doi: 10.1016/j.jcp.2011.09.021.
[22] Blades, E., Shah, P., Nucci, M., and Miskovish, S., "Demonstration of Multiphysics Analysis Tools on Representative Hypersonic Vehicle Structures," AIAA 2013-1746,, 2013. doi: 10.2514/6.2013-1746.
[23] Blades, E., Luke, E., and Ruf, J., "Fully Coupled Fluid-Structure Interaction Simulations of Rocket Engine Side Loads," AIAA-2012-3969, 2012. doi: 10.2514/6.2012-3969.
[24] Blades, E. L., and Cornish, A., "Aeroelastic Stability Predictions of a Business Jet Landing Gear Door using High Fidelity Fluid-Structure Interaction Tools", AIAA-2015-0173, 2015. doi: 10.2514/6.2015-0173.
[25] Luke, E., and George, T., ""Loci: A Rule-Based Framework for Parallel Multidisciplinary Simulation Synthesis,"" *Journal of Functional Programming*, Special Issue on Functional Approaches to High-Performance Parallel Programming, Vol. 15, No. 3, 2005, pp. 477-502.
[26] Luke, E., "On Robust and Accurate Arbitrary Polytope CFD Solvers (Invited)," AIAA 2007-39562007. doi: 10.2514/6.2007-3956.
[27] Bauchau, O.A., and Wang, J., "Efficient and Robust Approaches to the Stability Analysis of Large Multibody Systems," *Journal of Computational and Nonlinear Dynamics* Vol. 3, No. 1, January 2008.
[28] Auricchio, F., and E. Sacco, "A Superelastic Shape-Memory-Alloy Beam Model," *Journal of Intelligent Material Systems and Structures*, Vol. 8, No. 2, June 1997.